Anisotropic quantum transport in ZrSiS probed by high-field torque magnetometry

Duncan Miertschin,[1,*] Thinh Nguyen,[1,*] Shalika R. Bhandari,[2] Kyryl Shtefiienko,[1] Cole Phillips,[1] Birendra A. Magar,[3] Raman Sankar,[4] David E. Graf,[5,6] and Keshav Shrestha[1,†]

[1]*Department of Chemistry and Physics, West Texas A&M University, Canyon, Texas 79016, USA*
[2]*Department of Physics, Bhairahawa Multiple Campus, Tribhuvan University, Bhairahawa 32900, Nepal*
[3]*Department of Physics, New Mexico State University, Las Cruces, New Mexico 88003, USA*
[4]*Institute of Physics, Academia Sinica, Nankang, Taipei, 11529, Taiwan, Republic of China*
[5]*Department of Physics, Florida State University, Tallahassee, Florida 32306, USA*
[6]*National High Magnetic Field Laboratory, Tallahassee, Florida 32310, USA*

(Received 21 January 2024; revised 1 August 2024; accepted 2 August 2024; published 21 August 2024)

Here, we present electronic structures of the topological nodal line semimetal ZrSiS along in-plane and out-of-plane directions using high-field torque magnetometry. The torque signal measured up to 35 T exhibited clear de Haas-van Alphen (dHvA) oscillations in both directions; however, the angular dependence of the frequencies along these directions is quite different. Our Berry phase (Φ_B) calculations using the Landau level fan diagram show that $\Phi_B \approx \pi$, confirming the nontrivial topology of ZrSiS. Using Lifshitz-Kosevich and Dingle temperature analyses on the temperature and field-dependent dHvA oscillations data, we calculated all relevant physical parameters. We found that Dirac fermions exhibit anisotropic transport properties along the in-plane and out-of-plane directions, with in-plane fermions having a longer scattering time, a higher mean free path, and greater quantum mobility. To explain the experimental results, we computed the electronic bands and Fermi surface of ZrSiS using *ab initio* density functional theory. The electronic bands revealed multiple Dirac cones near the Fermi level, displaying linear dispersion over an energy range of 2 eV. The possible dHvA frequencies were computed using Onsager's relation, and the calculated frequencies closely align with the experimental dHvA frequencies. The anisotropic quantum transport properties presented here provide valuable insights into the unique Dirac fermion physics inherent in ZrSiS.

DOI: 10.1103/PhysRevB.110.085140

I. INTRODUCTION

The recent discovery of the topological phase in materials has attracted considerable interest in condensed matter physics [1–4]. A topological insulator (TI) represents a unique quantum state in materials, characterized by an insulating bulk and highly conductive surface states (SSs), arising from the nontrivial topology of the bulk state. TIs are theoretically predicted in materials with strong spin-orbit interactions and later experimentally verified in Bi-Te-Se compounds, also known as 3D TIs [5–8]. The SSs of 3D TIs show a distinct Dirac dispersion, with quasiparticles existing as massless Dirac fermions-wherein spin is entangled with momentum, forming a helical spin state [3,4]. SSs are robust and stable against disorder or impurities (excluding magnetic impurities) due to their topological protection [1]. These characteristics make TIs promising for applications in spintronics, low-power electronics, computer memory devices, and fast electronic devices.

Among the 3D systems displaying nontrivial topological states, topological nodal line (TNL) semimetals, featuring Dirac band crossings along a line or forming loops in momentum space, have garnered substantial attention due to their intriguing physics. Several compounds, such as $PtSn_4$ [9], $PbTaSe_2$ [10,11], ZrSiS [12,13], ZrSiSe/Te [14,15], and HfSiS [16,17], exhibit TNL behavior. Notably, ZrSiS distinguishes itself within this group by hosting multiple Dirac cones near the Fermi level, and its linear dispersion extends over a wide energy range of ∼2 eV [18,19]. Furthermore, high-quality single crystals of ZrSiS, stable in air, can be grown using relatively abundant, nontoxic elements through chemical vapor transport [20,21]. The unique electronic structure of ZrSiS makes it ideal for studying its electrical transport properties, which are expected to reveal complex and significant behaviors in its bulk states. Moreover, this material shows an exceptionally high magnetoresistance, reaching values as high as $\sim 10^5\%$ [21,22]. Hall measurements indicate that ZrSiS is a nearly electron-hole compensated system [23,24], explaining its remarkable magnetoresistance behavior. Additionally, it is found that this compound displays a negative longitudinal magnetoresistance when the current and magnetic fields are applied in the same direction [21].

The pressure effect on ZrSiS is also very intriguing. It undergoes two structural phase transitions occurring around 3.7 GPa and 18.7 GPa [25]. Moreover, this material exhibits tip-induced superconductivity while maintaining its topological properties, as observed in a point-contact electrical study [26]. Moreover, a recent quantum oscillation measurement under high pressure study by VanGennep *et al.* [27] revealed a possible pressure-induced topological quantum

*These authors contributed equally to this work.
†Contact author: kshrestha@wtamu.edu

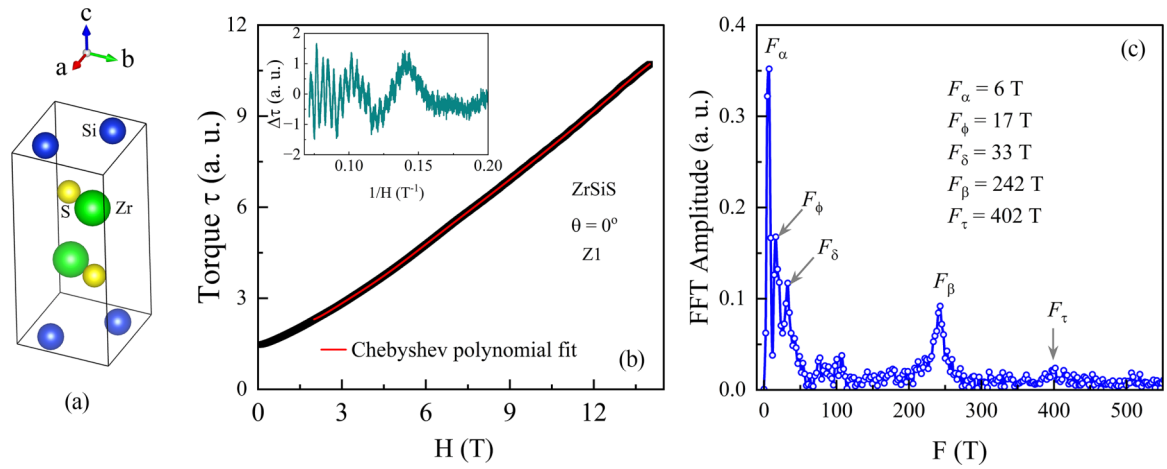

FIG. 1. (a) Unit cell of ZrSiS. (b) The torque τ vs H plot for ZrSiS single crystal Z1 with a field up to 14 T at $\theta = 0^\circ$ and $T = 1.5$ K. The red curve is the Chebyshev polynomial best fit curve. Inset: The background-subtracted torque $\Delta\tau$ vs $1/H$ plot. (c) The frequency spectrum of the torque data shown in (b). There are five distinct frequency peaks at 6 T, 17 T, 33 T, 242 T, and 402 T.

phase transition in this material at low pressures, occurring near (0.16 – 0.5) GPa. Applying chemical pressure [28] by replacing Zr with Hf in $Zr_{1-y}Hf_ySiS$, reveals two distinct Lifshitz transitions in the phase diagram, pointing to intriguing topology-related physics.

There has been extensive exploration of the electronic structure of this material through numerous quantum oscillation measurements [14,21,22,29–35]. However, most of these studies are carried out with the magnetic field along the *c* axis. There are limited studies [14,17] with the magnetic field along the *ab* plane. Furthermore, these studies with the field along the in-plane direction have been conducted only at a few tilt angles. For instance, the study by Gudac *et al.* [17] only measured at four angles (0°, 15°, 30°, and 45°). Similarly, Hu *et al.* [14] conducted torque measurements only at a fixed angle. Therefore, the electronic structure of ZrSiS with the magnetic field along the *ab* plane and the anisotropic nature of Dirac fermions in this compound have not been thoroughly explored.

In this paper, we present the electronic properties of ZrSiS using torque magnetometry with the applied field along both polar (θ) and azimuthal (ϕ) directions. Our torque measurements on four high-quality single crystals (Z1, Z2, Z3, and Z4) of ZrSiS, with maximum applied fields of up to 35 T, revealed clear dHvA oscillations in both directions. Our comprehensive analysis of the temperature and field-dependent data, using the Lifshitz-Kosevich (LK) and Dingle temperature calculations, showed that Dirac fermions in the in-plane and out-of-plane directions exhibit anisotropic features. Electronic band structures computed using *ab initio* density functional theory (DFT) revealed the presence of multiple Dirac cones near the Fermi level in ZrSiS. More importantly, our experimentally observed quantum oscillation frequencies are in good agreement with the first-principles calculations.

II. EXPERIMENTAL AND COMPUTATIONAL DETAILS

Large and high-quality single crystals of ZrSiS were synthesized using the chemical vapor transport method with iodine (I_2) as the transport agent. This material crystallizes in a tetragonal structure with the *P4/nmm* space group. The unit cell of ZrSiS is depicted in Fig. 1(a). Torque measurements with maximum magnetic fields up to 35 T and temperatures as low as 0.35 K were conducted at the National High Magnetic Field Laboratory in Tallahassee, Florida, using piezoresistive torque magnetometers. The magnetic field was rotated both in-plane and out-of-plane directions of the sample, with angles θ and ϕ, respectively, as illustrated in Figs. 2(a) and 3(a) insets. Magnetic fields were swept at each fixed temperature at a rate of 2 T/min. Electronic structures were computed using DFT with the full-potential linearized augmented plane wave (FP-LAPW) method within the WIEN2K code [36]. The details of the sample synthesis, experimental details, and first-principles calculations are presented in the Supplemental Material (SM) [37].

III. EXPERIMENTAL RESULTS

Figure 1(b) shows the magnetic torque (τ) for a ZrSiS single crystal Z1 with an applied field (H) up to 14 T at 1.5 K, measured at $\theta = 0^\circ$ (H//c). Here, θ represents the angle between the *c* axis and the applied field direction. The τ signal increases with H, however, the dHvA oscillations are not clearly visible. To extract dHvA oscillations, we fitted the Chebyshev polynomial to the torque data (the solid red line). The inset displays the background-subtracted torque data $\Delta\tau$ versus $1/H$ plot. As seen in the inset, dHvA oscillations are now clearly visible and there are multiple periods, indicating the presence of multiple frequencies. This can be confirmed by performing a fast Fourier transform (FFT) of the $\Delta\tau$ versus $1/H$ data. Figure 1(c) illustrates the frequency spectrum for the background-subtracted torque data of ZrSiS. The graph shows five distinct frequency peaks at $F_\alpha = 6$ T, $F_\phi = 17$ T, $F_\delta = 33$ T, $F_\beta = 242$ T, and $F_\tau = 402$ T. These frequencies are in good agreement with previously reported data [14,34]. Here, F_δ is nearly twice F_ϕ, but later we will show that F_δ originates from a distinct Fermi surface pocket. Moreover, F_τ is not clearly visible here, but it becomes more distinct at higher θ values and in another sample, Z2. It is important to note that $F_\alpha = 6$ T was not observed in previous

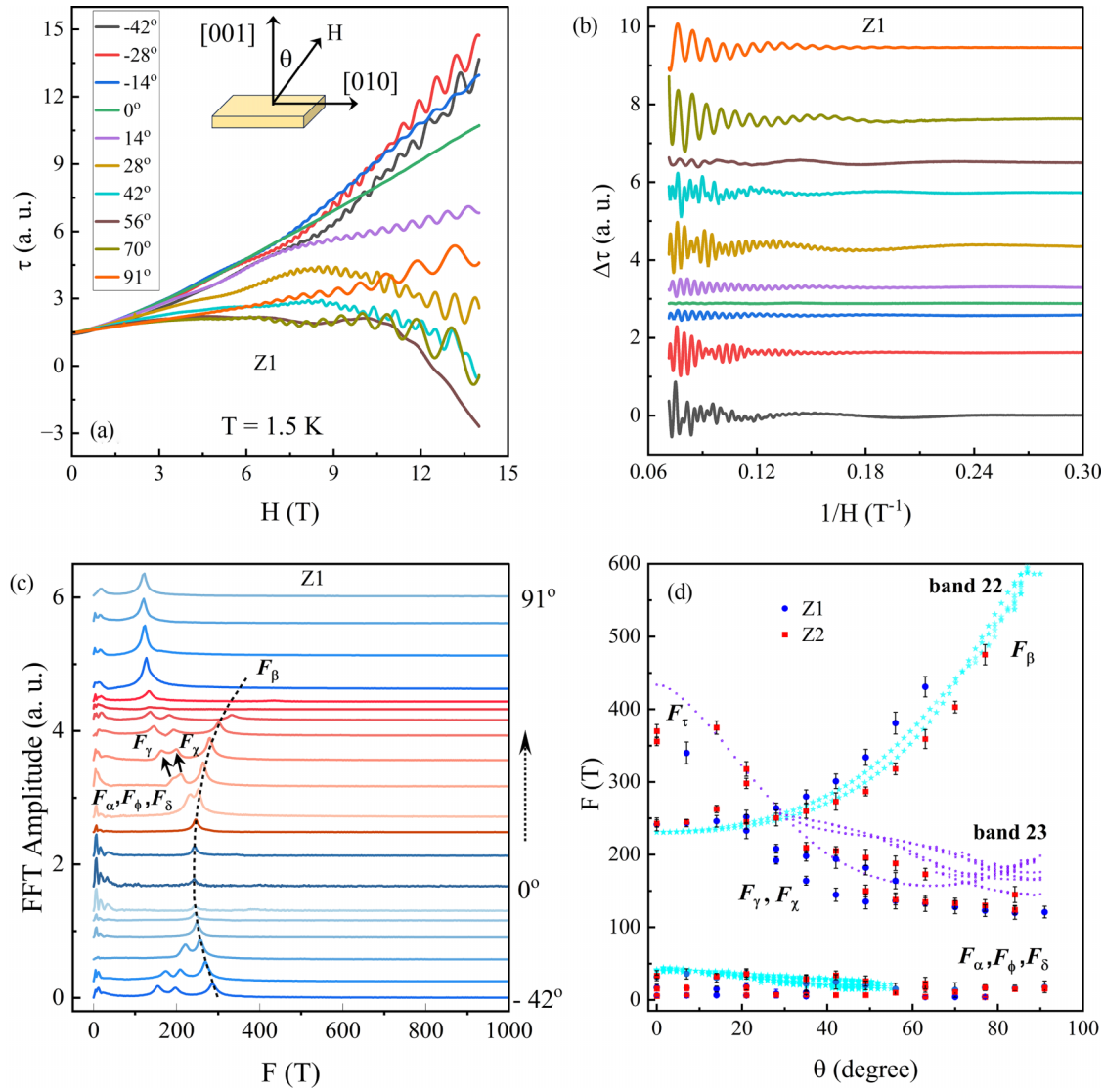

FIG. 2. Torque data on ZrSiS with the applied field along out of plane. (a) The torque versus H plot for ZrSiS single crystal Z1 at selected θ values at $T = 1.5$ K. Inset: A schematic showing the direction of sample rotation. (b) The background-subtracted dHvA oscillations, $\Delta\tau$ vs $1/H$ plot of the torque data shown in (a). (c) The frequency spectrum of ZrSiS at different θ values. The lowest curve is at $\theta = -42^\circ$, and each curve above it has an increment of 7°. The topmost curve represents the frequency at $\theta = 91^\circ$. The curves in (b) and (c) are shifted vertically and some of the curves are multiplied with a constant for clarity. The dashed curve is a guide to the eye. (d) The angular dependence of frequencies for two ZrSiS single crystals Z1 and Z2. Frequencies derived from DFT calculations for band 22 (cyan) and band 23 (purple) are shown as dotted curves.

magnetoresistance studies [20–22]. Electron transport in metals is governed by the scattering mechanism; hence, the Shubnikov–de Haas (SdH) oscillations in magnetoresistance originate from the oscillating rate, whereas dHvA oscillations arise directly from electrons' free energy [14,38]. Therefore, the absence of the F_α peak in SdH oscillations could be due to the low sensitivity of magnetotransport measurements.

At $\theta = 0^\circ$, the magnetic field is oriented along the c direction, i.e., [001], and at $\theta = 90^\circ$ the field aligns in the ab plane, as depicted in Fig. 2(a) inset. Figure 2(a) displays the torque data for ZrSiS at selected θ values ranging from -42° to 91°. The amplitude of dHvA oscillations varies with θ, which is more evident in the background-subtracted data shown in Fig. 2(b). The presence of quantum oscillations persists even when the magnetic field aligns parallel to the sample surface, indicating ZrSiS possesses a three-dimensional Fermi surface. Figure 2(c) depicts the angular dependence of quantum oscillation frequencies in ZrSiS with varying θ values. As depicted, both the number and position of frequencies vary with changes in θ. At $\theta = 0^\circ$, there are five dominant frequencies, $F_\alpha = 6$ T, $F_\delta = 17$ T, $F_\phi = 33$ T, $F_\beta = 242$ T, and $F_\tau = 402$ T. While increasing θ either positive or negative direction, F_α, F_δ, and F_ϕ remain nearly unchanged while F_β increases to higher values as guided by the dashed curve. It is important to note that other frequencies F_γ, F_χ, and F_τ gradually appear at higher θ values, as indicated by arrows. This angular dependence and emergence of additional frequencies at higher θ values in ZrSiS are consistent with previous MR and torque studies [21,22,33].

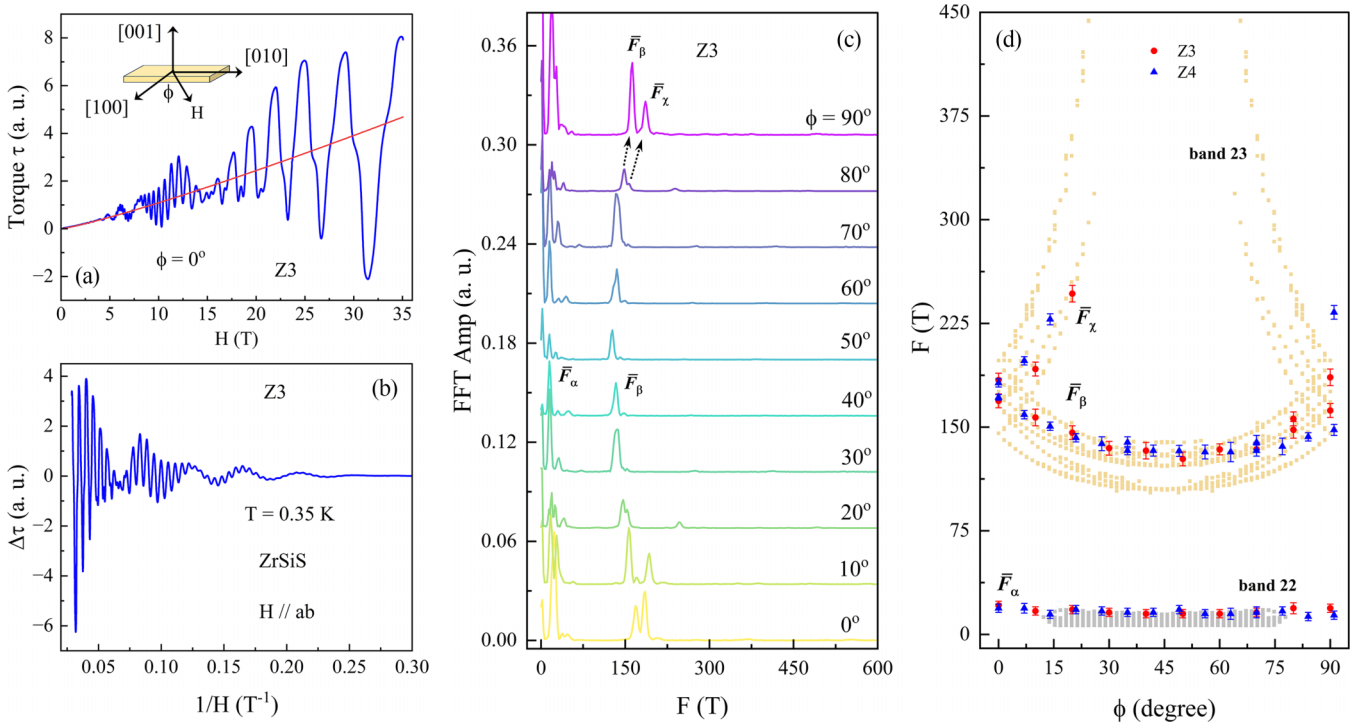

FIG. 3. Torque data on ZrSiS with the applied field along *ab* plane. (a) The torque signal of ZrSiS with the applied fields up to 35 T at $\phi = 0^\circ$ and $T = 0.35$ K. The red line shows a polynomial background fit to the data. Inset: A schematic showing the direction of sample rotation. (b) dHvA oscillations for ZrSiS after background subtraction. There are multiple periods in the dHvA oscillations. (c) The frequency spectrum of ZrSiS at different ϕ values. (d) The angular variation of frequencies for two ZrSiS single crystals Z3 and Z4. The frequency values from the DFT calculations (dotted curves) are also included for the comparison.

Figure 2(d) shows the angular dependence of frequencies for ZrSiS. Frequencies derived from torque measurements on another ZrSiS single crystal Z2 are also included in the plot for comparison. The detailed angle dependent torque data and frequency analyses for Z2 are shown in the SM [37] (Fig. S1). As seen in the graph, the dHvA frequencies derived from both Z1 and Z2 are comparable to one another. More importantly, the angular dependence of experimental frequencies are comparable with those extracted from the DFT calculations, which will be discussed later.

To probe the electronic properties along the out-of-plane direction, we conducted torque measurements with the field rotating in the *ab* plane. Figure 3(a) illustrates the torque data of ZrSiS single crystal Z3 with a maximum applied field of 35 T at $\phi = 0^\circ$. Here, ϕ is defined as the angle between the [100] direction and the direction of the applied field, as depicted in the Fig. 3(a) inset. The red curve represents the polynomial fit to the data. The oscillation exhibits multiple periods, as evident in the background-subtracted torque data shown in Fig. 3(b), indicating the presence of more than one frequency. Figure 3(c) shows the frequency spectrum of ZrSiS from $\phi = 0^\circ$ to 90°. The spectrum demonstrates two dominant frequencies $\bar{F}_\alpha$ and $\bar{F}_\beta$. For instance, at $\phi = 40^\circ$, two frequencies, $\bar{F}_\alpha = 15$ T and $\bar{F}_\beta = 133$ T, are present, closely matching the values from the previous in-plane torque measurement report [17] of ∼15 T and 125 T measured at $\phi = 45^\circ$. As we approach 0° or 90°, a new frequency $\bar{F}_\chi$ begins to appear, indicated by the dotted arrow. The angular dependence of frequencies for Z3 and Z4 is depicted in Fig. 3(d). The raw data and frequency analyses for the Z4 sample are presented in the SM [37] (Fig. S2). As shown in the graph, $\bar{F}_\alpha$, $\bar{F}_\beta$, and $\bar{F}_\chi$ for both Z3 and Z4 are comparable. While $\bar{F}_\alpha$ remains relatively unchanged, $\bar{F}_\beta$ varies almost parabolically with ϕ, reaching a minimum value near $\phi = 45^\circ$. $\bar{F}_\chi$ appears to diverge near $\phi = 45^\circ$ when approaching from either 0° or 90°. This angular variation of the frequencies can be explained by the DFT-calculated frequencies derived from the Fermi surface pockets of bands 22 and 23, which will be discussed in detail later.

It is noteworthy that the angular dependence of F_β and $\bar{F}_\beta$ is quite different [Figs. 2(d) and 3(d)]. Furthermore, despite applying magnetic fields of 35 T, we only detected two frequencies ($\bar{F}_\alpha$ and $\bar{F}_\beta$) below 300 T. In contrast, prior torque measurements [30–32] under 35 T reported numerous frequency peaks spanning from a few teslas to several kiloteslas, attributing their findings to magnetic breakdown phenomena. However, in our study, we didn't observe any indications of magnetic breakdown, simplifying the fermiology of ZrSiS.

To identify the topological state in ZrSiS, we have calculated the Berry phase (Φ_B) of the Fermi surface pocket corresponding to $\bar{F}_\beta$ using the Landau level (LL) fan plot [1,38]. For a topologically nontrivial (or trivial) system, the Φ_B value is π (or zero), as indicated by Refs. [1,25]. In Fig. 3, there are multiple frequencies present in the data, making it difficult to calculate Φ_B. To resolve this, we employed the FFT bandpass filter approach to extract the oscillations corresponding to the particular frequency. Assuming the magnetization (M) is perpendicular to the external field, the perpendicular component

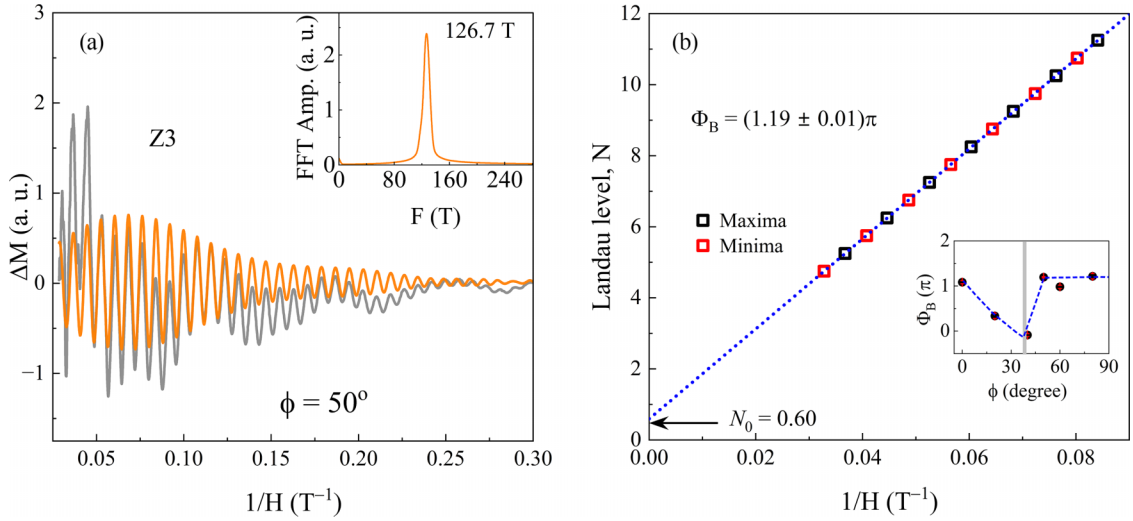

FIG. 4. (a) The extraction of dHvA oscillations corresponding to the frequency of 126 T using the FFT band-pass filter in ZrSiS. The gray curve represents the raw data at $\phi = 50^\circ$, while the orange curve depicts the filtered signal using a band-pass filter of (117 T – 135 T). Inset: The frequency spectrum of the filtered data. (b) The Landau level fan diagram for ZrSiS. The minimum and maximum positions in quantum oscillations are designated as $N - \frac{1}{4}$ and $N + \frac{1}{4}$, respectively. Inset: Angular dependence of Φ_B. The dotted line and the gray line are guides for the eye.

of M can be determined from the torque (τ) data using the formula $\vec{\tau} \propto \vec{M} \times \vec{H}$. We selected the data at $\phi = 50^\circ$ so $\bar{F}_\beta$ is well separated from other frequencies. The gray curve shows the raw magnetization data at $\phi = 50^\circ$ and the orange one represents the filtered data with the FFT bandpass filter of (117 T–135 T). The filtered signal consists of only one frequency of 126.7 T as shown in the Fourier transform data (inset).

Figure 4(b) illustrates the LL fan diagram for $\bar{F}_\beta$. When constructing this diagram, we assigned the LL index for the minima and maxima positions as $(N - \frac{1}{4})$ and $(N + \frac{1}{4})$ [38,39]. By performing a linear extrapolation of the data, represented by the dashed line, we derived an intercept of $N_o = 0.60 \pm 0.01$. This intercept corresponds to $\Phi_B = (1.19 \pm 0.01)\pi$, signifying the nontrivial topology of the β pocket. The slope value (126.6 ± 0.1)T closely matches $\bar{F}_\beta = 126.7$ T at $\phi = 50^\circ$, validating the precision of the linear extrapolation in determining the intercept (and consequently the Φ_B value). Furthermore, the bandpass filter's effectiveness in retaining the original dHvA oscillation signal without significant error is affirmed.

The application of high fields (35 T) leads the charge carriers to reach the fifth LL (near the quantum limit $N = 0$), a notable difference from $N = 26$ under 14 T (in Figs. 1 and 2). Bringing the Fermi pocket close to the quantum limit is essential for accurately determining Φ_B. Hence, the Φ_B value obtained through linear extrapolation in the LL fan diagram here is considered more reliable and precise. These findings regarding the nontrivial topology in ZrSiS for the β pocket are consistent with previously published results [14,21,27]. It is important to note that Φ_B decreases from approximately π at 0° to around 0 at 40°, and then returns to approximately π at 50° and higher angles, as shown in Fig. 4(b) inset. This highly tunable Φ_B has been observed in the Weyl semimetal WP_2 [40]; however, a detailed theoretical study is required to explain the origin of this behavior.

The temperature dependence of quantum oscillations can be described by the LK formula, allowing us to estimate the effective mass (m^*) of the charge carriers [38]. According to the LK theory, the temperature dependence of dHvA oscillations is given by

$$\Delta\tau(T, H) \propto e^{-\lambda_D} \frac{\lambda(T/H)}{\sinh[\lambda(T/H)]}, \tag{1}$$

with $\lambda_D(H) = \frac{2\pi^2 k_B}{\hbar e} m^* \frac{T_D}{H}$ and $\lambda(T/H) = \frac{2\pi^2 k_B}{\hbar e} m^* \frac{T}{H}$. Here, T_D, k_B, and m^* represent the Dingle temperature, Boltzmann's constant, and effective mass of the charge carriers, respectively. The first term is the Dingle factor, which describes the attenuation of the oscillations with decreasing field H. The second term explains the weakening of the oscillations at higher temperatures.

To determine m^*, we have measured dHvA oscillations on ZrSiS sample Z4 at different temperatures, as presented in Fig. S3 in the SM [37]. The temperature dependence of dHvA frequencies is displayed in Fig. 5(a). The amplitude of $\bar{F}_\alpha = 15$ T and $\bar{F}_\beta = 136$ T decreases at higher temperatures [Fig. 5(a) inset]. The solid curves represent the best-fit curves using the LK formula. From the best fit parameters, we estimated $m^*_\alpha = 0.06 m_e$ and $m^*_\beta = 0.09\ m_e$ for the α and β pockets, respectively, where m_e is the bare mass of a free electron. These m^* values are comparable to those reported by Hu *et al.* [14] but smaller than values reported in other studies [21,22,29,32] for ZrSiS. Furthermore, Figs. 5(b) and 5(c) represent the Dingle temperature analyses for the α and β pockets, respectively. From the best-linear fit, we obtained $T_D = 21.7$ K and 33.9 K for the α and β pockets, respectively.

Using the values of m^* and T_D, we have calculated all the physical parameters characterizing the α and β pockets, as presented in Table I. We have included data for H//c from Ref. [14] for comparison. As seen in the table, the mobility of

TABLE I. Physical parameters: frequency (F), Fermi wave vector (k_F), effective mass (m^*), Fermi velocity (v_F), Dingle temperature T_D, quantum relaxation time (τ_s), mean free path (l_{2D}), and quantum mobility (μ), of ZrSiS along in-plane and out-of-plane directions. The Fermi surface parameters for $H//c$ are adapted from Ref. [14].

Field	F(T)	$k_F(10^{-2}$Å$^{-1})$	m^*/m_o	$v_F(10^5$ ms$^{-1})$	T_D(K)	τ_s(ps)	l_{2D}(nm)	μ(cm^{2}V^{-1}s^{-1})
$H//ab$	15	2.1	0.06	4.1	21.7	0.06	2.29	1634
	136	6.4	0.09	8.2	33.9	0.04	2.94	697.3
	8.4	1.6	0.025	7.4	8.8	0.14	10.13	10,000
$H//c$	240	8.5	0.052	18.9	6	0.2	38.20	6,868
	17.6	2.3	0.027	9.88	14	0.084	8.54	5,469
	24.5	2.7	0.045	6.99	11.3	0.108	7.49	4,219

charge carriers in the in-plane direction is much larger-nearly ten times larger-than that in the out-of-plane direction.

IV. DFT CALCULATIONS

To better understand the electronic structure of ZrSiS and explain our high field torque data, we have conducted electronic band structure and Fermi surface analyses using the DFT calculations. Figure 6(a) displays electronic bands of ZrSiS taking into account of the spin-orbit coupling (SOC) effect. Electronic band structure without the SOC effect is presented in Fig. S4 in the SM [37]. There are multiple Dirac cones near the Fermi level as indicated by the dotted circles. Notably, the linear band dispersion spans nearly 2 eV, for instance, the Dirac cone along the A-Z direction. Due to the application of the SOC, a narrow gap ~ 0.02 eV opens up the Dirac spectrum. Two bands 22 and 23, cross the Fermi level and they are responsible for the Fermi surface of ZrSiS. Figures 6(b) and 6(c) illustrate the top and side views of ZrSiS's Fermi surface, respectively, exhibiting a cagelike structure within the $k_x - k_y$ plane and openness along the k_z direction. These electronic band structures and Fermi surface characteristics are consistent with previous studies [18,19,22,30].

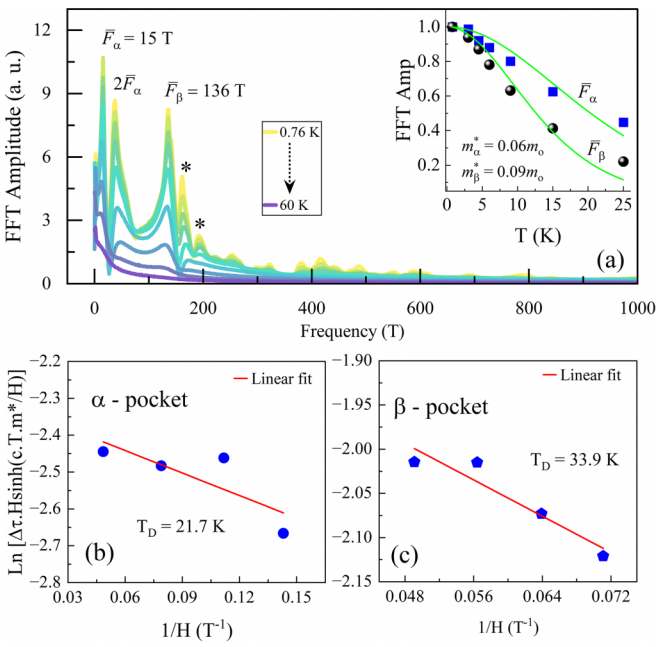

FIG. 5. (a) The FFT spectrum for the ZrSiS sample Z4 at different temperatures measured at $\phi = 42^\circ$. Inset: The temperature dependence of the FFT amplitude for the α and β pockets. The solid curves are the best fit using the LK formula [25,38]. There are a few additional peaks, indicated by asterisks, which appear only at $\phi = 42^\circ$ and 49°, and thus have not been considered for the LK analyses. The Dingle temperature analyses for the (b) α and (c) β pockets.

To compare with the experimental data, we measured the area of each energy isosurface forming the Fermi surface and then computed the oscillatory frequencies using the Onsager relation [41]. Utilizing the SKEAF code [42], we calculated all potential frequencies derived from each electronic band contributing to the formation of the Fermi surface in ZrSiS, considering both in-plane and out-of-plane directions. The calculated angular dependence of frequencies from bands 22 and 23 is depicted in Figs. 2(d) and 3(d), alongside the experimental data. Experimentally, we observed five major frequencies for $\theta = 0^\circ$ with the values of $F_\alpha = 6$ T, $F_\phi = 17$ T, $F_\delta = 33$ T, $F_\beta = 242$ T, and $F_\tau = 402$ T. The hole pocket derived from band 22 contributes two frequencies 40 T and 232 T, which are closer to the experimentally observed frequencies, namely, F_δ and F_β. Similarly, the electron pocket derived from band 23 contributes one frequency of 433 T, which is in good agreement with F_τ. The origin of experimentally observed frequencies from the possible orbits is depicted in Fig. 6(c). Furthermore, as seen in Fig. 2(d), the angular variation of F_δ, F_β, and F_τ aligns with the frequencies derived from the orbits δ, β, and τ, respectively. It is important to note that our DFT calculations could not generate the frequencies F_α and F_ϕ. This is due to our computational limitations, which prevented us from generating the entire section of the electron pocket. By using high k-points, Müller *et al.* [30] obtained the complete features of the Fermi surface and showed that these low frequencies near 8 T and 16 T can be derived from small cross sections of the electron pocket, which they denoted as δ_1 and δ_2. Similarly, the angular dependence of $\bar{F}_\beta$ and $\bar{F}_\chi$ matches the frequencies computed from band 23, whereas that of $\bar{F}_\alpha$ corresponds to the frequencies derived from band 22 [Fig. 3(d)].

V. SUMMARY

This paper presents a comprehensive study of the electronic properties of ZrSiS in both the in-plane and out-of-plane directions with the maximum applied fields of 35 T.

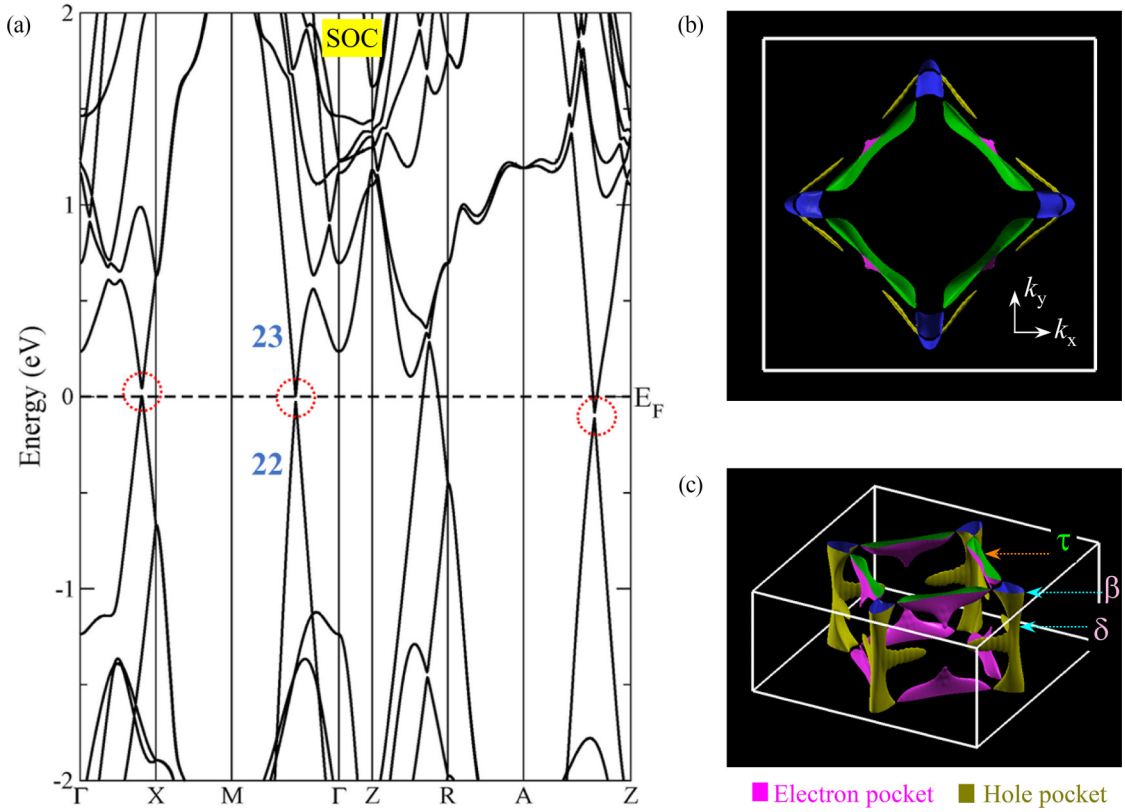

FIG. 6. (a) Electronic band structure of ZrSiS along high-symmetry directions, taking the spin-orbit coupling (SOC) effect into account. Multiple Dirac cones are present near the Fermi level, as indicated by dotted circles. The linear bands extend over a wide energy range (∼ 2 eV). Two bands (22 and 23) cross the Fermi level. (b) Top and (c) side views of the calculated Fermi surfaces. The dotted arrows depict the identified orbits that produce the observed quantum oscillation frequencies when the magnetic field is in the out-of-plane direction.

Despite several reports on quantum oscillations in this material, a thorough investigation of the Fermi surface in the out-of-plane direction has been lacking. Our detailed angular-dependent dHvA oscillation measurements, conducted with applied fields of up to 35 T, reveal that the oscillation frequencies vary anisotropically along both the polar and azimuthal directions [Figs. 2(d) and 3(d)]. Furthermore, using the LK analyses, we found that the scattering time for charge carriers in the out-of-plane direction is nearly five times shorter than that for the charge carriers in the in-plane direction, despite their nearly comparable effective masses. This anisotropic scattering rate results in a smaller mean free path in the out-of-plane direction and subsequently leads to nearly ten times lower mobility in the out-of-plane direction (Table I). In layered materials like ZrSiS, there is weak out-of-plane bonding compared to the strong in-plane bonding, resulting in anisotropic electronic properties. Therefore, the anisotropic properties observed in Table 1 for ZrSiS are due to its layered structure.

Our Berry phase calculation through the Landau level fan plot near the quantum limit clearly shows that ZrSiS is a topologically nontrivial system. However, the Berry phase exhibits an angle dependence, and its physical origin remains to be explored. To explain our experimental findings, we performed electronic band structure and Fermi surface calculations using *ab initio* DFT. Two electronic bands intersecting the Fermi level significantly contribute to ZrSiS's Fermi surface. Importantly, the angular dependence of the observed dHvA oscillation frequencies is consistent with those computed using DFT. The detailed electronic properties, both in-plane and out-of-plane, presented in this paper will be significantly important for understanding the fermiology of ZrSiS and other nodal line semimetals.

ACKNOWLEDGMENTS

The research at West Texas A&M University (WTAMU) is supported by the Killgore Faculty Research program, the Killgore Undergraduate and Graduate Student Research Grants, and the Welch Foundation (Grant No. AE-0025). This work relied on computations performed on the WTAMU HPC cluster, which was funded by the National Science Foundation (NSF CC* GROWTH 2018841). R.S. acknowledges financial support provided by the Ministry of Science and Technology in Taiwan under Projects No. NSTC 111-2124-M-001-007, No. 113-2112-M-001-045-MY3, and Academia Sinica Project No. AS-iMATE-113-12. A portion of this work was performed at the National High Magnetic Field Laboratory, which is supported by National Science Foundation Cooperative Agreement No. DMR-2128556 and the State of Florida.

[1] Y. Ando, J. Phys. Soc. Jpn. **82**, 102001 (2013).

[2] B. R. Ortiz, P. M. Sarte, E. M. Kenney, M. J. Graf, S. M. L. Teicher, R. Seshadri, and S. D. Wilson, Phys. Rev. Mater. **5**, 034801 (2021).

[3] X.-L. Qi and S.-C. Zhang, Rev. Mod. Phys. **83**, 1057 (2011).

[4] M. Z. Hasan and C. L. Kane, Rev. Mod. Phys. **82**, 3045 (2010).

[5] Y. Xia, D. Qian, D. Hsieh, L. Wray, A. Pal, H. Lin, A. Bansil, D. Grauer, Y. S. Hor, R. J. Cava *et al.*, Nat. Phys. **5**, 398 (2009).

[6] A. A. Taskin and Y. Ando, Phys. Rev. B **84**, 035301 (2011).

[7] Y. Ando and L. Fu, Annu. Rev. Condens. Matter Phys. **6**, 361 (2015).

[8] K. Shrestha, V. Marinova, B. Lorenz, and P. C. W. Chu, Phys. Rev. B **90**, 241111(R) (2014).

[9] Y. Wu, L.-L. Wang, E. Mun, D. D. Johnson, D. Mou, L. Huang, Y. Lee, S. L. Bud'ko, P. C. Canfield, and A. Kaminski, Nat. Phys. **12**, 667 (2016).

[10] G. Bian, T.-R. Chang, R. Sankar, S.-Y. Xu, H. Zheng, T. Neupert, C.-K. Chiu, S.-M. Huang, G. Chang, I. Belopolski *et al.*, Nat. Commun. **7**, 10556 (2016).

[11] K. Yokoi, H. Murakawa, H. Sakai, and N. Hanasaki, Phys. Rev. B **106**, 115118 (2022).

[12] L. M. Schoop, M. N. Ali, C. Straßer, A. Topp, A. Varykhalov, D. Marchenko, V. Duppel, S. S. Parkin, B. V. Lotsch, and C. R. Ast, Nat. Commun. **7**, 11696 (2016).

[13] M. Neupane, I. Belopolski, M. M. Hosen, D. S. Sanchez, R. Sankar, M. Szlawska, S.-Y. Xu, K. Dimitri, N. Dhakal, P. Maldonado, P. M. Oppeneer, D. Kaczorowski, F. Chou, M. Z. Hasan, and T. Durakiewicz, Phys. Rev. B **93**, 201104(R) (2016).

[14] J. Hu, Z. Tang, J. Liu, Y. Zhu, J. Wei, and Z. Mao, Phys. Rev. B **96**, 045127 (2017).

[15] R. J. Kirby, L. Muechler, S. Klemenz, C. Weinberg, A. Ferrenti, M. Oudah, D. Fausti, G. D. Scholes, and L. M. Schoop, Phys. Rev. B **103**, 205138 (2021).

[16] D. Takane, Z. Wang, S. Souma, K. Nakayama, C. X. Trang, T. Sato, T. Takahashi, and Y. Ando, Phys. Rev. B **94**, 121108(R) (2016).

[17] B. Gudac, M. Bosnar, F. Orbanić, T. Ivšić, I. Kokanović, and M. Novak, SciPost Phys. Proc. **11**, 019 (2023).

[18] C.-C. Su, C.-S. Li, T.-C. Wang, S.-Y. Guan, R. Sankar, F. Chou, C.-S. Chang, W.-L. Lee, G.-Y. Guo, and T.-M. Chuang, New J. Phys. **20**, 103025 (2018).

[19] A. N. Rudenko and S. Yuan, Phys. Rev. B **101**, 115127 (2020).

[20] R. Sankar, G. Peramaiyan, I. P. Muthuselvam, C. J. Butler, K. Dimitri, M. Neupane, G. N. Rao, M.-T. Lin, and F. Chou, Sci. Rep. **7**, 40603 (2017).

[21] R. Singha, A. K. Pariari, B. Satpati, and P. Mandal, Proc. Natl. Acad. Sci. **114**, 2468 (2017).

[22] M. N. Ali, L. M. Schoop, C. Garg, J. M. Lippmann, E. Lara, B. Lotsch, and S. S. Parkin, Sci. Adv. **2**, e1601742 (2016).

[23] Y.-Y. Lv, B.-B. Zhang, X. Li, S.-H. Yao, Y. Chen, J. Zhou, S.-T. Zhang, M.-H. Lu, and Y.-F. Chen, Appl. Phys. Lett. **108**, 244101 (2016).

[24] J. Zhang, M. Gao, J. Zhang, X. Wang, X. Zhang, M. Zhang, W. Niu, R. Zhang, and Y. Xu, Front. Phys. **13**, 137201 (2018).

[25] R. Singha, S. Samanta, S. Chatterjee, A. Pariari, D. Majumdar, B. Satpati, L. Wang, A. Singha, and P. Mandal, Phys. Rev. B **97**, 094112 (2018).

[26] L. Aggarwal, C. K. Singh, M. Aslam, R. Singha, A. Pariari, S. Gayen, M. Kabir, P. Mandal, and G. Sheet, J. Phys.: Condens. Matter **31**, 485707 (2019).

[27] D. VanGennep, T. A. Paul, C. W. Yerger, S. T. Weir, Y. K. Vohra, and J. J. Hamlin, Phys. Rev. B **99**, 085204 (2019).

[28] B. Gudac, M. Kriener, Y. V. Sharlai, M. Bosnar, F. Orbanić, G. P. Mikitik, A. Kimura, I. Kokanović, and M. Novak, Phys. Rev. B **105**, L241115 (2022).

[29] X. Wang, X. Pan, M. Gao, J. Yu, J. Jiang, J. Zhang, H. Zuo, M. Zhang, Z. Wei, W. Niu *et al.*, Adv. Electron. Mater. **2**, 1600228 (2016).

[30] C. S. A. Müller, T. Khouri, M. R. van Delft, S. Pezzini, Y.-T. Hsu, J. Ayres, M. Breitkreiz, L. M. Schoop, A. Carrington, N. E. Hussey, and S. Wiedmann, Phys. Rev. Res. **2**, 023217 (2020).

[31] F. Orbanić, M. Novak, Z. Glumac, A. McCollam, L. Tang, and I. Kokanović, Phys. Rev. B **103**, 045122 (2021).

[32] S. Pezzini, M. Van Delft, L. Schoop, B. Lotsch, A. Carrington, M. Katsnelson, N. E. Hussey, and S. Wiedmann, Nat. Phys. **14**, 178 (2018).

[33] Y. Yang, H. Xing, G. Tang, C. Hua, C. Yao, X. Yan, Y. Lu, J. Hu, Z. Mao, and Y. Liu, Phys. Rev. B **103**, 125160 (2021).

[34] M. Matusiak, J. Cooper, and D. Kaczorowski, Nat. Commun. **8**, 15219 (2017).

[35] J. A. Voerman, L. Mulder, J. C. de Boer, Y. Huang, L. M. Schoop, C. Li, and A. Brinkman, Origin of the butterfly magnetoresistance in ZrSiS, Phys. Rev. Mater. **3**, 084203 (2019).

[36] P. Blaha, K. Schwarz, G. K. Madsen, D. Kvasnicka, and J. Luitz *et al.*, *WIEN2k: An Augmented Plane Wave Plus Local Orbitals Program for Calculating Crystal Properties* (Vienna University of Technology, Austria, 2001), Vol. 60.

[37] See Supplemental Material at http://link.aps.org/supplemental/10.1103/PhysRevB.110.085140 for detailed information on sample synthesis, computational method, temperature and field-dependent torque data, electronic band structure, and more, and which includes J. P. Perdew, K. Burke and M. Ernzerhof, Phys. Rev. Lett. **77**, 3865 (1996) and K. Koepernik and H. Eschrig, Phys. Rev. B **59**, 1743 (1999).

[38] D. Shoenberg, *Magnetic Oscillations in Metals* (Cambridge University Press, Cambridge, 1984).

[39] K. Shrestha, R. Chapai, B. K. Pokharel, D. Miertschin, T. Nguyen, X. Zhou, D. Y. Chung, M. G. Kanatzidis, J. F. Mitchell, U. Welp, D. Popović, D. E. Graf, B. Lorenz, and W. K. Kwok, Phys. Rev. B **105**, 024508 (2022).

[40] K. Zhang, Y. Du, P. Wang, L. Wei, L. Li, Q. Zhang, W. Qin, Z. Lin, B. Cheng, Y. Wang *et al.*, Chin. Phys. Lett. **37**, 090301 (2020).

[41] According to the Onsager's relation, the quantum oscillation measured frequency of an electron orbit (F) which is perpendicular to the applied magnetic field is related to the area of the Fermi surface (A) by $F = \frac{\phi_0}{2\pi^2}A$, where $\phi_0 = 2.07 \times 10^{-15}\,\mathrm{Tm}_2$ is the quantum of flux.

[42] S. Julian, Comput. Phys. Commun. **183**, 324 (2012).